

ARTICLE

<https://doi.org/10.1038/s41467-019-09061-9>

OPEN

A complex hydride lithium superionic conductor for high-energy-density all-solid-state lithium metal batteries

Sangryun Kim¹, Hiroyuki Oguchi², Naoki Toyama¹, Toyoto Sato¹, Shigeyuki Takagi¹, Toshiya Otomo³, Dorai Arunkumar¹, Naoaki Kuwata⁴, Junichi Kawamura⁴ & Shin-ichi Orimo^{1,2}

All-solid-state batteries incorporating lithium metal anode have the potential to address the energy density issues of conventional lithium-ion batteries that use flammable organic liquid electrolytes and low-capacity carbonaceous anodes. However, they suffer from high lithium ion transfer resistance, mainly due to the instability of the solid electrolytes against lithium metal, limiting their use in practical cells. Here, we report a complex hydride lithium superionic conductor, $0.7\text{Li}(\text{CB}_9\text{H}_{10})\text{-}0.3\text{Li}(\text{CB}_{11}\text{H}_{12})$, with excellent stability against lithium metal and a high conductivity of $6.7 \times 10^{-3} \text{ S cm}^{-1}$ at 25°C . This complex hydride exhibits stable lithium plating/stripping reaction with negligible interfacial resistance ($<1\Omega\text{ cm}^2$) at 0.2 mA cm^{-2} , enabling all-solid-state lithium-sulfur batteries with high energy density ($>2500\text{ Wh kg}^{-1}$) at a high current density of 5016 mA g^{-1} . The present study opens up an unexplored research area in the field of solid electrolyte materials, contributing to the development of high-energy-density batteries.

¹ Institute for Materials Research, Tohoku University, 2-1-1 Katahira, Aoba-ku, Sendai 980-8577, Japan. ² WPI-Advanced Institute for Materials Research (WPI-AIMR), Tohoku University, 2-1-1 Katahira, Aoba-ku, Sendai 980-8577, Japan. ³ Institute of Materials Structure Science, High Energy Accelerator Research Organization, 1-1 Oho, Tsukuba 305-0801, Japan. ⁴ Institute of Multidisciplinary Research for Advanced Materials, Tohoku University, 2-1-1 Katahira, Aoba-ku, Sendai 980-8577, Japan. Correspondence and requests for materials should be addressed to S.K. (email: sangryun@imr.tohoku.ac.jp) or to S.-i.O. (email: orimo@imr.tohoku.ac.jp)

All-solid-state batteries are promising candidates for resolving the intrinsic drawbacks of current lithium-ion batteries, such as electrolyte leakage, flammability, and limited energy density^{1–3}. Recent extensive research on all-solid-state batteries has led to considerable progress in solid electrolytes, which are generally categorized into sulfide solid electrolytes and oxide solid electrolytes. The most attractive feature of sulfide solid electrolytes, such as Li₁₀GeP₂S₁₂-type compounds^{1,4,5}, Li₂S–P₂S₅ glass ceramics^{2,6}, and argyrodites^{7,8}, is their high lithium ion conductivity of over 10^{–3} S cm^{–1} at room temperature, which is comparable to those of liquid electrolytes. Oxide solid electrolytes such as perovskite-type^{9,10} and garnet-type^{11,12} materials have been also found to be promising due to their high processing flexibility and air stability.

Despite tremendous research advancements in solid electrolytes, the development of all-solid-state batteries for practical applications, such as electric vehicles and grid-scale energy storage systems, is still in its infancy, mainly in terms of energy density. This has stimulated research into combining suitable high-energy-density electrodes with solid electrolytes. In this regard, lithium metal is the ultimate anode material for all-solid-state batteries because it has the highest theoretical capacity (3860 mAh g^{–1}) and the lowest potential (–3.04 V vs. standard hydrogen electrode) among known anode materials. However, most existing solid electrolytes have chemical/electrochemical instability and/or poor physical contact against lithium metal, inevitably causing unwanted side reactions at the interface^{13–15}. These side reactions result in an increase in interfacial resistance, greatly degrading battery performance during repeated cycling. Efforts have been made to overcome these shortcomings, including alloying the lithium metal anode^{16,17} and introducing buffer layers^{3,18,19}. However, lithium metal alloys have higher potential than that of pure lithium metal, lowering the cell voltage and thus energy density. In addition, buffer layers increase cell resistance due to their lower conductivities compared to those of solid electrolytes. It is thus desirable to find a solid electrolyte that is intrinsically stable and compatible with lithium metal to maximize the advantages of the lithium metal anode.

Complex hydrides, generally denoted as $M_x(M'yH_z)$, where M represents a metal cation and M'yH_z represents a complex anion, have received particular attention as a new class of solid electrolytes to address the problems associated with the lithium metal anode owing to their high deformability and outstanding chemical/electrochemical stability against the lithium metal anode, which results from their high reducing ability^{20,21}. However, the major drawback of complex hydrides is their low ionic conductivity (~10^{–5} S cm^{–1} at room temperature), thus requiring high-temperature (~100 °C) operation for stable battery performance^{20,22,23}. Therefore, the development of complex hydride solid electrolytes that exhibit high ionic conductivity at room temperature will be a revolutionary breakthrough for all-solid-state batteries employing a lithium metal anode.

In this work, we develop a complex hydride lithium superionic conductor from a solid solution of two complex hydrides, namely Li(CB₉H₁₀) and Li(CB₁₁H₁₂). The partial replacement of (CB₉H₁₀)[–] with (CB₁₁H₁₂)[–] stabilizes the disordered high-temperature (high-T) phase of Li(CB₉H₁₀) at lower temperatures, leading to a lithium superionic conductivity of 6.7 × 10^{–3} S cm^{–1} at 25 °C. This material shows unparalleled stability with lithium metal and thus has a variety of advantages as the solid electrolyte for all-solid-state lithium metal batteries even near room temperature, allowing high lithium ion transfer capability at the interface with the lithium metal anode and stable cycling of high-energy-density all-solid-state lithium-sulfur (Li–S) batteries.

Results

Material synthesis and characterization. A complex hydride lithium superionic conductor was synthesized by stabilizing the disordered high-T phase of a *closo*-type complex hydride containing *closo*-type (cage-like) complex anions (Supplementary Fig. 1 and Supplementary Note 1) at room temperature. In this study, Li(CB₉H₁₀) was chosen as the host starting material for the stabilization of the high-T phase because of its low phase transition temperature (90 °C) and high lithium ion conductivity, approaching 10^{–1} S cm^{–1} for the high-T phase²⁴. The stabilization of the high-T phase of Li(CB₉H₁₀) was achieved by partially replacing (CB₉H₁₀)[–] complex anions with (CB₁₁H₁₂)[–] complex anions using a mechanical ball-milling technique (see the Methods section for details). (CB₁₁H₁₂)[–] complex anions were used as they have similar geometry and size and the same valence compared to those of (CB₉H₁₀)[–] complex anions. The phase transition temperatures and ionic conductivities of *closo*-type complex hydrides are summarized in Supplementary Table 1. Additional descriptions of the starting materials (Li(CB₉H₁₀) and Li(CB₁₁H₁₂)), including the geometries of (CB₉H₁₀)[–] and (CB₁₁H₁₂)[–] complex anions (Supplementary Fig. 1), X-ray diffraction (XRD) patterns (Supplementary Fig. 2), field-emission scanning electron microscopy (FE-SEM) images (Supplementary Fig. 3), and differential thermal analysis (DTA) profiles (Supplementary Fig. 4), are provided in the Supplementary Information.

From the testing of various (CB₁₁H₁₂)[–] complex anion content levels, a 0.3 molar fraction of (CB₁₁H₁₂)[–] was chosen as the main composition (denoted as 0.7Li(CB₉H₁₀)–0.3Li(CB₁₁H₁₂)) for stabilizing the high-T phase of Li(CB₉H₁₀), as lower content (0.1 molar fraction) resulted in the incomplete stabilization of the high-T phase and higher content (0.5 molar fraction) led to the formation of other impurity phases (Supplementary Fig. 5 and Supplementary Note 2). The XRD pattern of 0.7Li(CB₉H₁₀)–0.3Li(CB₁₁H₁₂) shows new diffraction peaks that are not assigned to the low-temperature (low-T) phases of the starting materials (Fig. 1a, Supplementary Figs. 6 and 7, and Supplementary Note 3). These peaks were indexed by the hexagonal unit cell, which is consistent with that (space group *P*31*c* (*Z* = 2)²⁴) of the high-T phase of Li(CB₉H₁₀). The estimated unit cell volume per formula unit (V/*Z* = 219 Å³) of 0.7Li(CB₉H₁₀)–0.3Li(CB₁₁H₁₂) is larger than that of Li(CB₉H₁₀) (V/*Z* = 205 Å³) (Supplementary Table 2), revealing the formation of a solid-solution phase of Li(CB₉H₁₀) and Li(CB₁₁H₁₂), in which the centres of (CB₉H₁₀)[–] and (CB₁₁H₁₂)[–] occupy the same sites (2*b* = (1/3, 2/3, *z*)) in the crystal structure. The expanded lattice is consistent with the substitution of the larger (CB₁₁H₁₂)[–] for the smaller (CB₉H₁₀)[–]. These results verify that the high-T phase of Li(CB₉H₁₀) is stabilized at room temperature by the partial substitution of complex anions. The lowered phase transition temperature can be possibly attributed to the increased entropy change due to the effects of the formation of the solid-solution phase, by which disordered distributions of both lithium ions and complex anions are thermodynamically preferred.

The phase transition between the low-T and high-T phases was investigated by DTA (Fig. 1b and Supplementary Table 1). The DTA profile of Li(CB₉H₁₀) cycled between 25 and 200 °C exhibits endothermic and exothermic peaks at 90 and 80 °C upon heating–cooling cycling, which originate from the reversible transitions to and from the disordered high-T phase²⁴. Importantly, 0.7Li(CB₉H₁₀)–0.3Li(CB₁₁H₁₂) displays no such endothermic and exothermic peaks, reconfirming the stabilization of the high-T phase at room temperature. Additionally, the high thermal stability of 0.7Li(CB₉H₁₀)–0.3Li(CB₁₁H₁₂) was verified by XRD measurements after the heat-treatment at 473 K for 12 h (Supplementary Fig. 8).

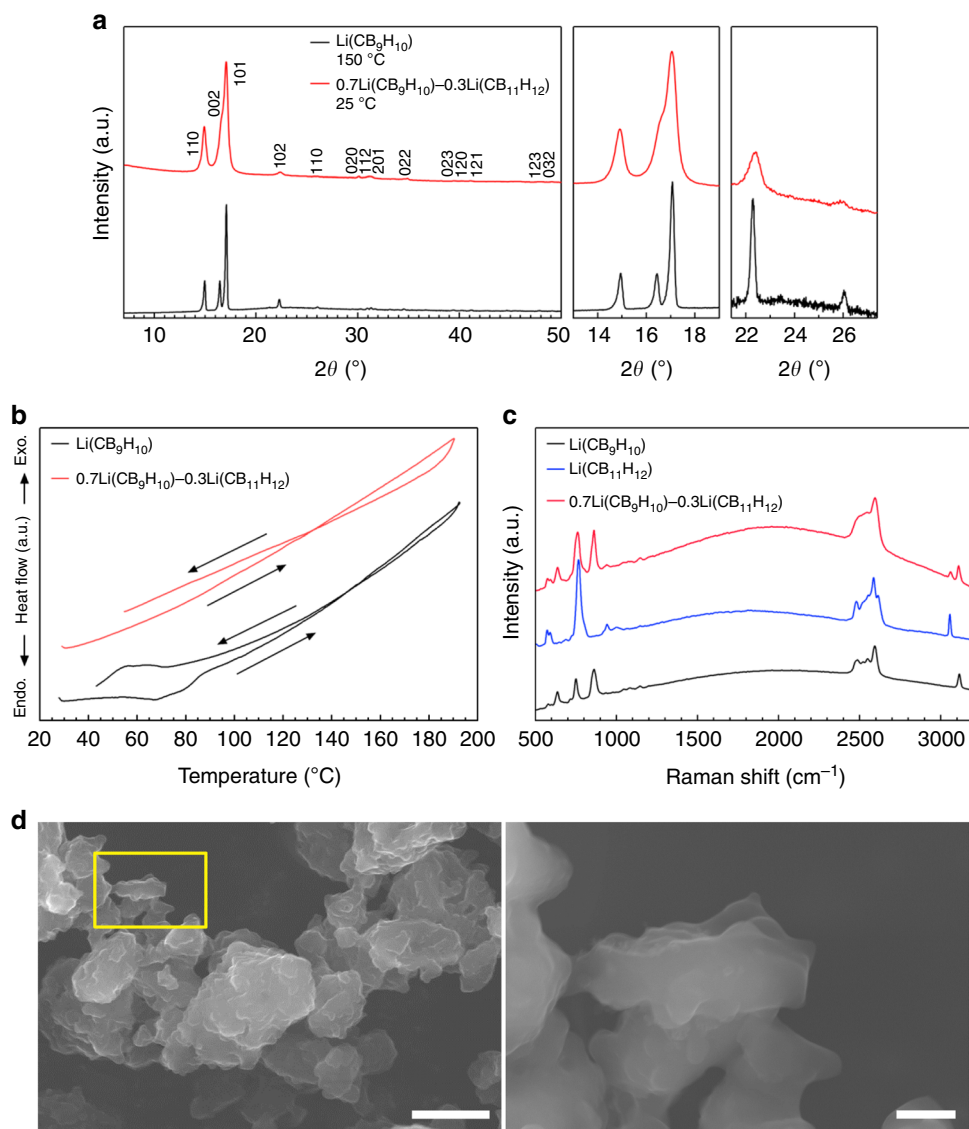


Fig. 1 Stabilization of high-*T* phase at room temperature. **a** XRD patterns of Li(CB₉H₁₀) at 150 °C and 0.7Li(CB₉H₁₀)–0.3Li(CB₁₁H₁₂) at room temperature. **b** DTA curves of Li(CB₉H₁₀) and 0.7Li(CB₉H₁₀)–0.3Li(CB₁₁H₁₂). **c** Raman spectra of Li(CB₉H₁₀), Li(CB₁₁H₁₂), and 0.7Li(CB₉H₁₀)–0.3Li(CB₁₁H₁₂). **d** FE-SEM images of 0.7Li(CB₉H₁₀)–0.3Li(CB₁₁H₁₂). The magnified image (right) is of the yellow marked area (left). Scale bars, 20 μm for the left image in **d** and 3 μm for the right image in **d**.

The vibrational modes of complex anions in 0.7Li(CB₉H₁₀)–0.3Li(CB₁₁H₁₂) were examined by Raman spectroscopy measurements (Fig. 1c). In the low-Raman-shift region below 1200 cm⁻¹, the Raman profile of 0.7Li(CB₉H₁₀)–0.3Li(CB₁₁H₁₂) exhibits various deformation vibration modes²⁵ of both (CB₉H₁₀)⁻ and (CB₁₁H₁₂)⁻. In addition, Raman peaks at 3110 and 3050 cm⁻¹, which are ascribed to C-H stretching modes²⁵ in (CB₉H₁₀)⁻ and (CB₁₁H₁₂)⁻, respectively, were observed for 0.7Li(CB₉H₁₀)–0.3Li(CB₁₁H₁₂). These results indicate that (CB₉H₁₀)⁻ and (CB₁₁H₁₂)⁻ remain intact and coexist in the solid-solution phase.

FE-SEM images of 0.7Li(CB₉H₁₀)–0.3Li(CB₁₁H₁₂) depict that the prepared sample forms secondary particles with sizes of 10–20 μm consisting of primary particles of imperfect circular morphology with sizes of 1–3 μm (Fig. 1d and Supplementary Fig. 9). The primary particles were interconnected with very smooth edges. These morphologies reflect the softness and deformability of the prepared sample, which can allow close contact with electrode materials during cell preparation.

Lithium ion conductivity. The ionic conductivity of 0.7Li(CB₉H₁₀)–0.3Li(CB₁₁H₁₂) was assessed using electrochemical impedance spectroscopy (EIS) measurements with Au electrodes. For the measurements, the pelletized samples were prepared by cold-pressing at 153.6 MPa. To provide a reference for a quantitative comparison, the results for Li(CB₉H₁₀) are also shown²⁴. The impedance profile of Li(CB₉H₁₀) at 25 °C (=298 K) exhibits one semicircle in the high-frequency region and one spike in the low-frequency region (Fig. 2a), which correspond to contributions from the bulk/grain boundary and the electrode, respectively. In contrast, 0.7Li(CB₉H₁₀)–0.3Li(CB₁₁H₁₂) displays only one spike, which is ascribed to the electrode contribution. The impedance of 0.7Li(CB₉H₁₀)–0.3Li(CB₁₁H₁₂), which includes bulk and grain boundary resistances, was determined from the intercept of the electrode spike on the Z-axis. Of note, the impedance measured for 0.7Li(CB₉H₁₀)–0.3Li(CB₁₁H₁₂) is orders of magnitude lower compared to that of Li(CB₉H₁₀). The lithium ion conductivity (σ) at 25 °C of 0.7Li(CB₉H₁₀)–0.3Li(CB₁₁H₁₂) is 6.7×10^{-3} S cm⁻¹, which is three

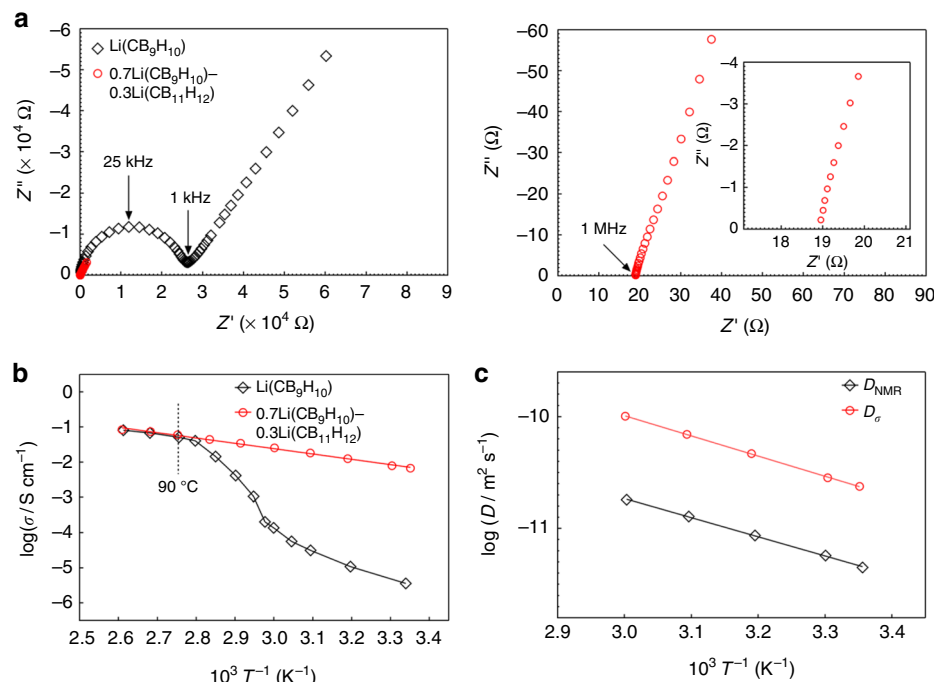


Fig. 2 Lithium ion conductivity of 0.7Li(CB₉H₁₀)–0.3Li(CB₁₁H₁₂). **a** Nyquist plots of Li(CB₉H₁₀) and 0.7Li(CB₉H₁₀)–0.3Li(CB₁₁H₁₂) at 25 °C (left). Magnified Nyquist plots of 0.7Li(CB₉H₁₀)–0.3Li(CB₁₁H₁₂) in the high-frequency region (right). **b** Arrhenius plots of the lithium ion conductivities of Li(CB₉H₁₀) and 0.7Li(CB₉H₁₀)–0.3Li(CB₁₁H₁₂). **c** Arrhenius plots of the diffusion coefficients calculated from the impedance and NMR measurements

orders of magnitude higher than that ($\sigma = 3.6 \times 10^{-6} \text{ S cm}^{-1}$) of Li(CB₉H₁₀).

An Arrhenius plot of ionic conductivities shows that as the temperature increases from 25 to 90 °C, Li(CB₉H₁₀) displays a drastic jump in ionic conductivity, which originates from a transition to the high- T phase (Fig. 2b, Supplementary Fig. 10a, and Supplementary Note 4). In contrast, for 0.7Li(CB₉H₁₀)–0.3Li(CB₁₁H₁₂), the Arrhenius plot shows no phase-transition-derived changes in conductivity and a linear increase in the logarithmic values (Fig. 2b and Supplementary Fig. 10b). Importantly, at above 90 °C, the conductivities of 0.7Li(CB₉H₁₀)–0.3Li(CB₁₁H₁₂) match well with those of Li(CB₉H₁₀): the conductivities at 110 °C and activation energies (E_a) of Li(CB₉H₁₀) and 0.7Li(CB₉H₁₀)–0.3Li(CB₁₁H₁₂) are $8.1 \times 10^{-2} \text{ S cm}^{-1}$ and 28.9 kJ mol^{-1} , and $8.5 \times 10^{-2} \text{ S cm}^{-1}$ and 28.4 kJ mol^{-1} , respectively (Supplementary Table 1 and Supplementary Note 5). It has been reported that the fast ionic conduction in the high- T phase of complex hydrides results from their vacancy-rich disordered cation sublattices within networks of reorientationally disordered complex anions^{24,26–29}.

⁷Li-pulsed field gradient nuclear magnetic resonance (PFG-NMR) analyses indicate that the self-diffusion coefficient (D_{NMR}) of 0.7Li(CB₉H₁₀)–0.3Li(CB₁₁H₁₂) is lower than the conductivity diffusion coefficient (D_{σ}) calculated from the impedance measurements (Fig. 2c, Supplementary Fig. 11, and Supplementary Note 6). The Haven ratio, $H_R = D_{\text{NMR}}/D_{\sigma}$, was ~0.17 in the temperature range of 25–60 °C, clarifying that the high ionic conductivity of 0.7Li(CB₉H₁₀)–0.3Li(CB₁₁H₁₂) is the result of a strong correlation between highly disordered lithium ions, which induces concerted ionic diffusion^{30–32}.

To the best of our knowledge, the room-temperature conductivity ($6.7 \times 10^{-3} \text{ S cm}^{-1}$ at 25 °C) of 0.7Li(CB₉H₁₀)–0.3Li(CB₁₁H₁₂) is the highest value reported to date for complex hydride lithium ion conductors (Fig. 3). This conductivity is comparable to those of oxide-based^{9,11} and sulfide-based^{2,4,7} solid electrolytes. Considering that organic liquid electrolytes³³ have transport numbers of below 0.5,

0.7Li(CB₉H₁₀)–0.3Li(CB₁₁H₁₂) has higher conductivity than organic liquid electrolytes.

Stability against lithium metal anode. 0.7Li(CB₉H₁₀)–0.3Li(CB₁₁H₁₂) shows markedly high stability against the lithium metal anode in terms of potential window, interfacial resistance, voltage polarization, and lithium plating/stripping cycling. Electrochemical stability was first evaluated by cyclic voltammetry (CV) with a Mo/0.7Li(CB₉H₁₀)–0.3Li(CB₁₁H₁₂)/Li cell at 25 °C (Fig. 4a and Supplementary Fig. 12). The cell displays sharp and reversible cathodic and anodic currents at around 0 V, which correspond to lithium deposition ($\text{Li}^+ + \text{e}^- \rightarrow \text{Li}$) and dissolution ($\text{Li} \rightarrow \text{Li}^+ + \text{e}^-$), respectively, revealing the high reducing ability of 0.7Li(CB₉H₁₀)–0.3Li(CB₁₁H₁₂). In addition, the lack of oxidation currents within the scanned voltage range (−0.1 to 5 V) demonstrates the wide potential window of 0.7Li(CB₉H₁₀)–0.3Li(CB₁₁H₁₂).

The interfacial resistance between 0.7Li(CB₉H₁₀)–0.3Li(CB₁₁H₁₂) and the lithium metal anode was investigated using the EIS measurement with a symmetric Li/0.7Li(CB₉H₁₀)–0.3Li(CB₁₁H₁₂)/Li cell at 25 °C (Fig. 4b). The impedance profile of the Li/0.7Li(CB₉H₁₀)–0.3Li(CB₁₁H₁₂)/Li cell displays one semicircle in the high-frequency region and one spike in the low-frequency region, which correspond to contributions from the 0.7Li(CB₉H₁₀)–0.3Li(CB₁₁H₁₂)/Li interface and the electrode, respectively (Supplementary Fig. 13, Supplementary Table 3, and Supplementary Note 7). The 0.7Li(CB₉H₁₀)–0.3Li(CB₁₁H₁₂)/Li interfacial resistance was calculated to be $0.78 \Omega \text{ cm}^2$. This interfacial resistance is quite noticeable, as it is far lower than those of other solid electrolyte/Li interfaces reported to date^{3,14,16,18,19,34–37}. The interfacial resistances between the solid electrolyte and the lithium metal anode are summarized in Supplementary Table 4. An FE-SEM image confirms close physical contact at the interface between 0.7Li(CB₉H₁₀)–0.3Li(CB₁₁H₁₂) and lithium metal (Fig. 4c). The remarkable interfacial

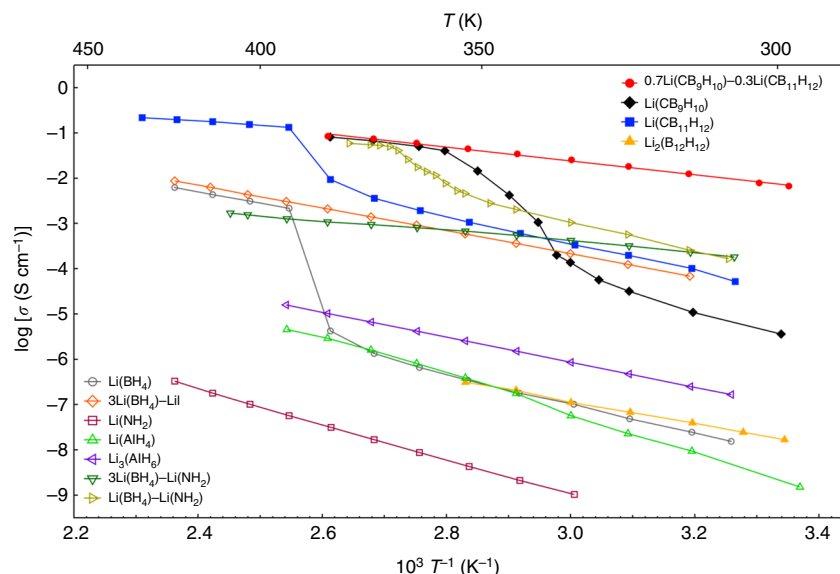


Fig. 3 Arrhenius plots of the conductivities of $0.7\text{Li}(\text{CB}_9\text{H}_{10})\text{-}0.3\text{Li}(\text{CB}_{11}\text{H}_{12})$ and those of other complex hydride lithium ion conductors^{23,24,41-46}. $0.7\text{Li}(\text{CB}_9\text{H}_{10})\text{-}0.3\text{Li}(\text{CB}_{11}\text{H}_{12})$ exhibits a high lithium ion conductivity of $6.7 \times 10^{-3} \text{ S cm}^{-1}$ at 25 °C, which is the highest value reported for complex hydride lithium ion conductors

compatibility of $0.7\text{Li}(\text{CB}_9\text{H}_{10})\text{-}0.3\text{Li}(\text{CB}_{11}\text{H}_{12})$ with the lithium metal anode is ascribed to its high chemical stability and high physical deformability.

$0.7\text{Li}(\text{CB}_9\text{H}_{10})\text{-}0.3\text{Li}(\text{CB}_{11}\text{H}_{12})$ also shows extremely stable lithium ion transfer capability across the interface with the lithium metal anode. When galvanostatically cycled at a current density of 0.2 mA cm^{-2} in both directions for 30 min at 25 °C, the $\text{Li}/0.7\text{Li}(\text{CB}_9\text{H}_{10})\text{-}0.3\text{Li}(\text{CB}_{11}\text{H}_{12})/\text{Li}$ cell exhibited very small voltage polarization (6.0 mV) (Fig. 4d). More importantly, the $\text{Li}/0.7\text{Li}(\text{CB}_9\text{H}_{10})\text{-}0.3\text{Li}(\text{CB}_{11}\text{H}_{12})/\text{Li}$ cell shows superior voltage retention after repeated lithium plating and stripping cycles. At a current density of 0.2 mA cm^{-2} , no voltage changes were observed during 300 cycles (Fig. 4e and Supplementary Fig. 14). The low and unvaried interfacial resistances were also verified by EIS measurements (Supplementary Fig. 15). The superior lithium ion transfer performance confirms the high electrochemical stability of $0.7\text{Li}(\text{CB}_9\text{H}_{10})\text{-}0.3\text{Li}(\text{CB}_{11}\text{H}_{12})$ against the lithium metal anode.

All-solid-state lithium metal battery with complex hydride solid electrolyte. $0.7\text{Li}(\text{CB}_9\text{H}_{10})\text{-}0.3\text{Li}(\text{CB}_{11}\text{H}_{12})$ can potentially be used to realize a wide range of lithium-metal-based all-solid-state batteries. Based on the high ionic conductivity and high stability with lithium metal of $0.7\text{Li}(\text{CB}_9\text{H}_{10})\text{-}0.3\text{Li}(\text{CB}_{11}\text{H}_{12})$, the electrochemical investigation was expanded to all-solid-state full cells using $0.7\text{Li}(\text{CB}_9\text{H}_{10})\text{-}0.3\text{Li}(\text{CB}_{11}\text{H}_{12})$ as the solid electrolyte and lithium metal as the anode. As shown in Fig. 5a, a high-energy-density S electrode (theoretical capacity = 1672 mAh g⁻¹; working voltage = 2.1 V vs. Li^+/Li) was used as the cathode to take advantage of the high-energy density of the lithium metal anode. The cathode composite was prepared by mixing an S–carbon (C) composite and $0.7\text{Li}(\text{CB}_9\text{H}_{10})\text{-}0.3\text{Li}(\text{CB}_{11}\text{H}_{12})$ solid electrolyte. The all-solid-state batteries were fabricated by cold-pressing at 153.6 MPa. Detailed cell preparation and measurement conditions are described in the Methods section. Fig. 5b shows the voltage profiles recorded during the first two cycles measured in the voltage range of 1.0–2.5 V (vs. Li^+/Li) for a rate of 0.03 C (50.2 mA g^{-1}) at 25 °C. The C-rate is determined as follows: a rate of $n\text{C}$ means that the current will (dis)charge the full capacity in $1/n$ hours. In the first cycle, the

discharge capacity and the charge capacity were 2013 and 1557 mAh g⁻¹, respectively. The higher capacity in the first discharge is presumably attributed to the capacity contribution from the solid electrolyte³⁸. After the first discharge, reversible charge–discharge profiles, which present a charge plateau at around 2.2 V and a discharge plateau at around 2.0 V, were observed. The discharge capacity in the second cycle was 1618 mAh g⁻¹, which corresponds to 96.8% of the theoretical capacity.

After the first cycle, as the C-rate increased by 1.67, 3.33, 10, and 33.3 times from 0.03 C (1 C = 1672 mAh g⁻¹), the all-solid-state cell retained 96.5%, 90.0%, 81.4%, and 73.4% of its capacity (1618 mAh g⁻¹) in the second cycle, respectively (Fig. 5c, d). The all-solid-state cells also showed good cycling stability. At 0.1 C (Supplementary Fig. 16 and Supplementary Note 8) and 1 C (Fig. 5e and Supplementary Fig. 17), 98.9% and 84.4% of the capacity (1431 and 1239 mAh g⁻¹) in the second cycle was retained after 10 and 20 cycles, respectively. In addition, for a discharging rate of 3 C and a charging rate of 1 C at 50 °C, the discharge capacity was 1533 mAh g⁻¹ in the second cycle, and slightly dropped to 1469 mAh g⁻¹ after 20 cycles, leading to high-energy densities of 2578–2782 Wh kg⁻¹ (Fig. 5f and Supplementary Fig. 18). During cycling, the coulombic efficiencies became saturated at ~100% (Fig. 5e, f, and Supplementary Fig. 16b). From the perspective of energy density, the reversible energy densities of over 2500 Wh kg⁻¹ at high current densities of 1–3 C are remarkable, as they are better than those of previously reported $\text{Li}-\text{S}$ ^{22,38}, $\text{Li}-\text{LiCoO}_2$ ^{4,19,36}, $\text{Li}-\text{LiNi}_{0.5}\text{Mn}_{1.5}\text{O}_4$ ¹⁶, and $\text{Li}-\text{Li}_2\text{FeMn}_3\text{O}_8$ ³ all-solid-state batteries.

$0.7\text{Li}(\text{CB}_9\text{H}_{10})\text{-}0.3\text{Li}(\text{CB}_{11}\text{H}_{12})$ also presents the high stability during prolonged cycling. When cycled for a discharging rate of 5 C and a charging rate of 1 C at 60 °C, the discharge capacity was 1472 mAh g⁻¹ in the second cycle, and the reversible capacity of 1017 mAh g⁻¹ with the coulombic efficiency of ~100% was retained after 100 cycles (Fig. 6a and Supplementary Fig. 19). An FE-SEM image verifies the preserved intimate contact at the $0.7\text{Li}(\text{CB}_9\text{H}_{10})\text{-}0.3\text{Li}(\text{CB}_{11}\text{H}_{12})/\text{Li}$ interface after cycling (Fig. 6b). Furthermore, no dendrite growth was observed across the $0.7\text{Li}(\text{CB}_9\text{H}_{10})\text{-}0.3\text{Li}(\text{CB}_{11}\text{H}_{12})/\text{Li}$ interface. This physical stability was confirmed in multiple measurement regions (Fig. 6b and

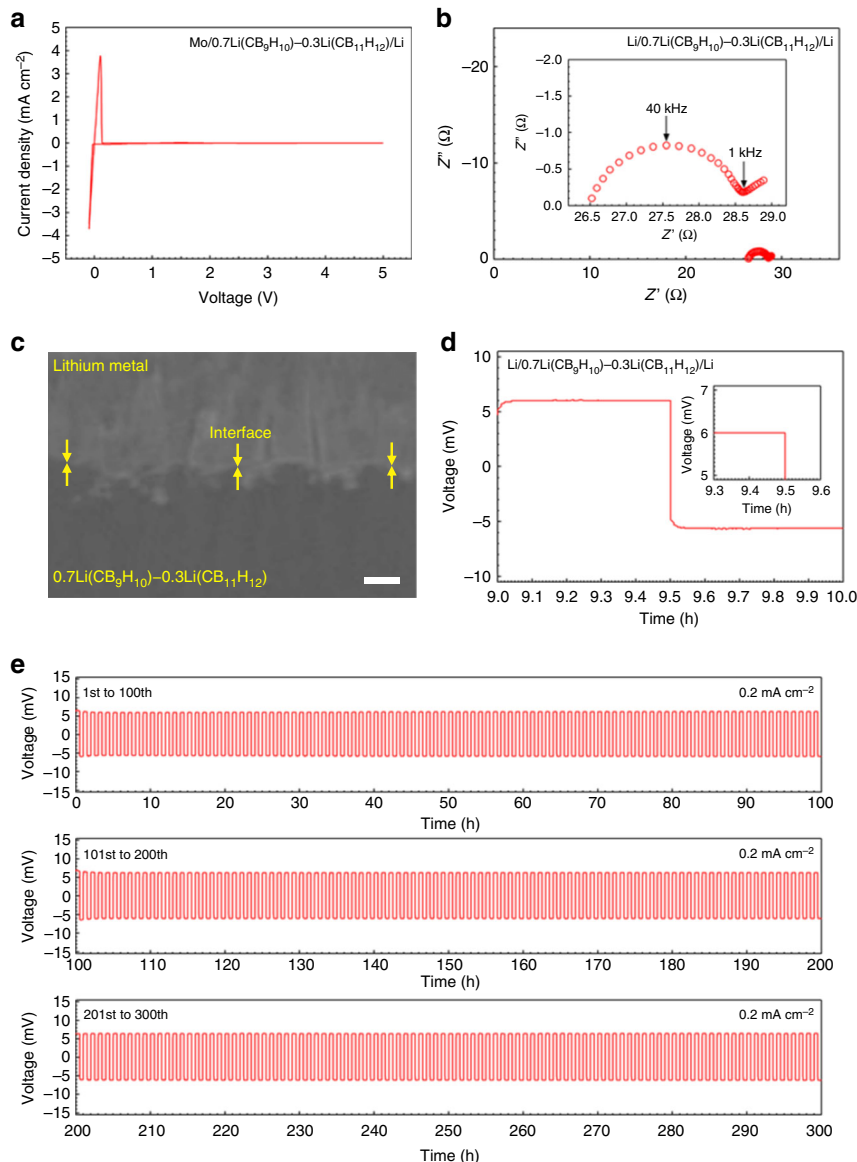


Fig. 4 Stability of 0.7Li(CB₉H₁₀)–0.3Li(CB₁₁H₁₂) with lithium metal. **a** CV curve of a Mo/0.7Li(CB₉H₁₀)–0.3Li(CB₁₁H₁₂)/Li cell at a scan rate of 0.5 mV s⁻¹ and a scan range of -0.1 to 5.0 V (vs. Li⁺/Li). **b** Nyquist plot of a Li/0.7Li(CB₉H₁₀)–0.3Li(CB₁₁H₁₂)/Li cell. Inset shows the magnified plot in the region of the semicircle indicating the 0.7Li(CB₉H₁₀)–0.3Li(CB₁₁H₁₂)/Li interfacial resistance. **c** FE-SEM image of the 0.7Li(CB₉H₁₀)–0.3Li(CB₁₁H₁₂)/Li interface. **d** 10th galvanostatic cycling profile of the Li/0.7Li(CB₉H₁₀)–0.3Li(CB₁₁H₁₂)/Li cell. Inset shows the magnified profile. **e** Galvanostatic cycling profiles for prolonged cycles. 1st–100th cycles (top), 101st–200th cycles (middle), and 201st–300th cycles (bottom). All electrochemical measurements were conducted at 25 °C. Scale bar, 30 μm in c

Supplementary Fig. 20). In addition, XRD (Fig. 6c) and Raman spectroscopy (Fig. 6d) measurements indicate that the characteristic peaks of 0.7Li(CB₉H₁₀)–0.3Li(CB₁₁H₁₂) are maintained after cycling. These results demonstrate the practical feasibility of the 0.7Li(CB₉H₁₀)–0.3Li(CB₁₁H₁₂) solid electrolyte for all-solid-state batteries employing the lithium metal anode.

Discussion

We developed the complex hydride lithium superionic conductor 0.7Li(CB₉H₁₀)–0.3Li(CB₁₁H₁₂). The partial incorporation of Li(CB₁₁H₁₂) into Li(CB₉H₁₀) allows the disordered high-*T* phase of Li(CB₉H₁₀) to stabilize at room temperature. As a result of the effects of the disordered complex hydride phase, a room-temperature lithium superionic conductivity of over 10⁻³ S cm⁻¹ was achieved for the first time for a pure complex hydride. Of note,

this study provides a general guideline for how to develop lithium superionic conductors based on *closو-type* complex hydrides: (1) find a host *closو-type* complex hydride that exhibits a high ionic conductivity in the disordered high-*T* phase, (2) find a *closو-type* complex anion whose structure and size are similar to those of the host material, and (3) partially incorporate the given complex anion into the host material to form a disordered structure, which stabilizes the high-*T* phase at lower temperatures.

The synthesis principle used in this study is different from those used previously for *closو-type* lithium ion conductors with multiple complex anions. Since previous approaches focused on synthetic methods without considerations of material compositions, the produced compounds contained a massive amount of residual products^{39,40} due to incomplete mixing of complex anions, complicating efforts to apply the conductors to batteries, as well as making precise analyses of conduction properties difficult.

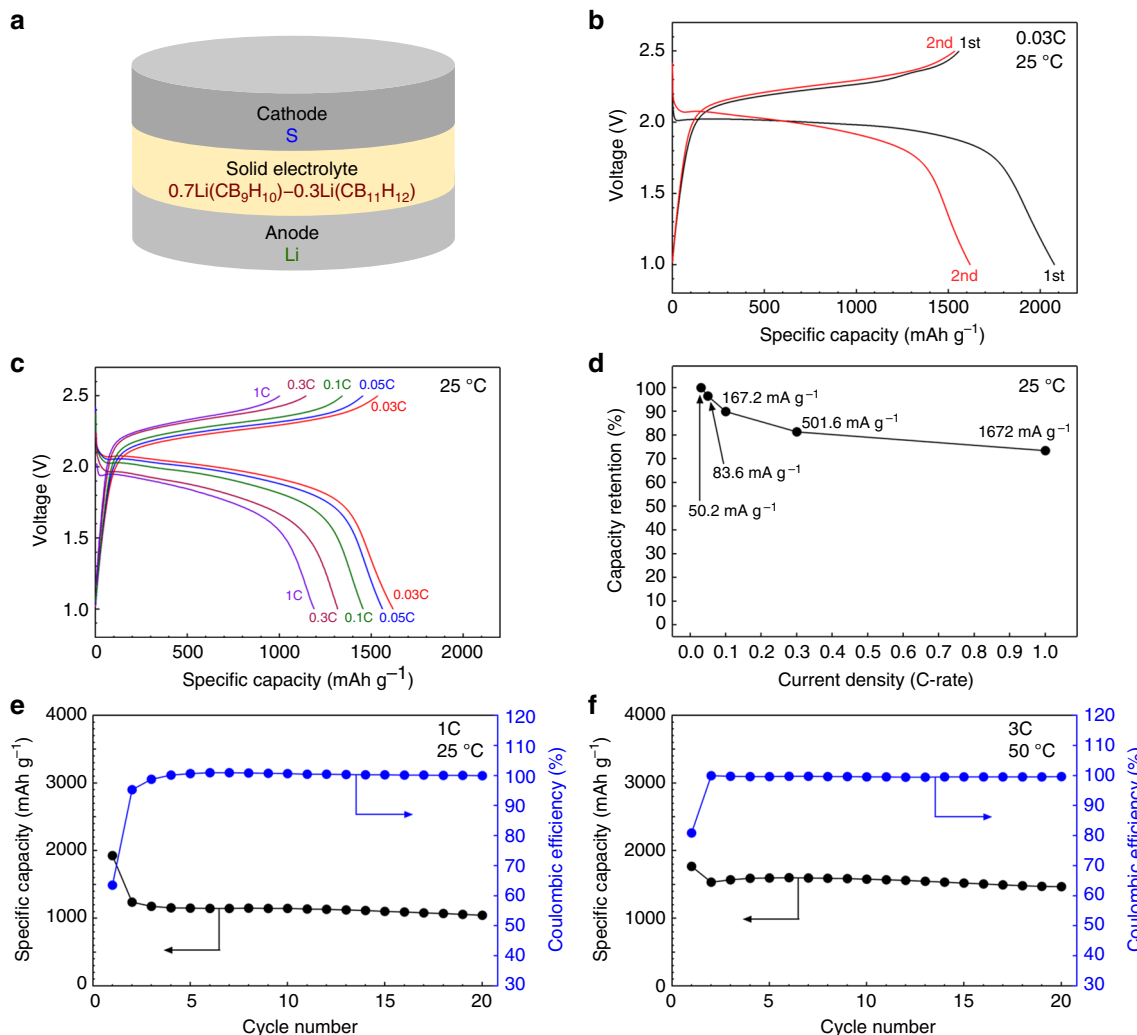


Fig. 5 High-energy-density all-solid-state lithium metal batteries. **a** Schematic illustration of the prepared all-solid-state batteries. S, Li/0.7Li(CB₉H₁₀)–0.3Li(CB₁₁H₁₂), and lithium metal were used as the cathodes, solid electrolytes, and anodes, respectively. **b** Voltage profiles for a rate of 0.03 C (50.2 mA g⁻¹) at 25 °C during the first two cycles. **c** Discharge-charge profiles at 0.03, 0.05, 0.1, 0.3, and 1 C after an initial cycle at 25 °C. **d** Capacity retention as a function of current density. **e, f** Cycling performances of discharge capacity and coulombic efficiency (**e**) for a rate of 1 C at 25 °C and (**f**) for a discharging rate of 3 C and a charging rate of 1 C at 50 °C

The developed *clos*-type complex hydride has various advantages as a solid electrolyte in all-solid-state batteries. Its intrinsic stability with the lithium metal anode enables facile and stable lithium ion transfer at the interface. The high ionic conductivity of 0.7Li(CB₉H₁₀)–0.3Li(CB₁₁H₁₂) coupled with its stability with lithium metal enables excellent performance of high-energy-density Li–S batteries in a wide temperature range. From the battery manufacturing perspective, the superior deformability of 0.7Li(CB₉H₁₀)–0.3Li(CB₁₁H₁₂) facilitates the preparation of compact solid electrolytes and electrode/electrolyte interface, resulting in intimate contact throughout the battery. The unique properties of the developed complex hydride solid electrolyte will not only inspire future efforts to find lithium superionic conductors based on complex hydrides, but also opens up a new group of solid electrolytes for practical all-solid-state lithium metal batteries that may lead to the development of high-energy-density electrochemical devices.

Methods

Synthesis. The starting materials, Li(CB₉H₁₀) and Li(CB₁₁H₁₂), were obtained by drying Li(CB₉H₁₀)·xH₂O (Katchem) at 200 °C for 12 h and Li(CB₁₁H₁₂)·xH₂O (Katchem) at 160 °C for 12 h under vacuum (<5 × 10⁻⁴ Pa). Li(CB₉H₁₀) and Li

(CB₁₁H₁₂) were weighted in the appropriate molar ratios and ground using a mortar and pestle for 15 min. To synthesize the (1-x)(CB₉H₁₀)–x0.3Li(CB₁₁H₁₂) ($x = 0.1, 0.3$, and 0.5) complex hydrides, the mixed powder was mechanically milled using a planetary ball mill (Pulverisette 7, Fritsch) with 20 steel balls (each 7 mm in diameter) at 400 rpm for 20 h. After ball-milling, the powders were reground using a mortar and pestle for 15 min. All of the procedures were conducted under an Ar atmosphere.

Characterization. The phase analysis was performed with XRD (XPERT Pro, PANalytical) measurements with CuK α radiation (wavelength $\lambda = 1.5406 \text{ \AA}$ for K α_1 and 1.5444 \AA for K α_2) in the 2θ range of 7–50°. The powder for the XRD measurements was loaded into a thin-walled glass capillary under an Ar atmosphere and sealed with paraffin liquid. DTA was performed using a Rigaku Thermo Plus TG-8120 system from 25 to 200 °C at a ramping rate of 5 °C min⁻¹ under an Ar flow (150 cc min⁻¹). The vibrational modes of complex anions were characterized by Raman spectroscopy (DXR, Thermo Scientific). Morphologies and particle sizes were analyzed using FE-SEM (SU9000, Hitachi).

Ionic conductivity measurement. Fifty milligrams of the powder was first placed into a 10-mm-diameter Teflon guide and uniaxially pressed at 153.6 MPa to prepare the pellet-type sample (0.10 cm in thickness and 0.785 cm² in surface area). Subsequently, Au electrode powders were transferred onto both sides of the pressed sample still present in the Teflon guide and uniaxially pressed again at 153.6 MPa to obtain a single pellet comprising the solid electrolyte and Au electrodes. No additional sintering process was conducted to reduce grain boundaries before measurements. Ionic conductivities were measured using the AC impedance

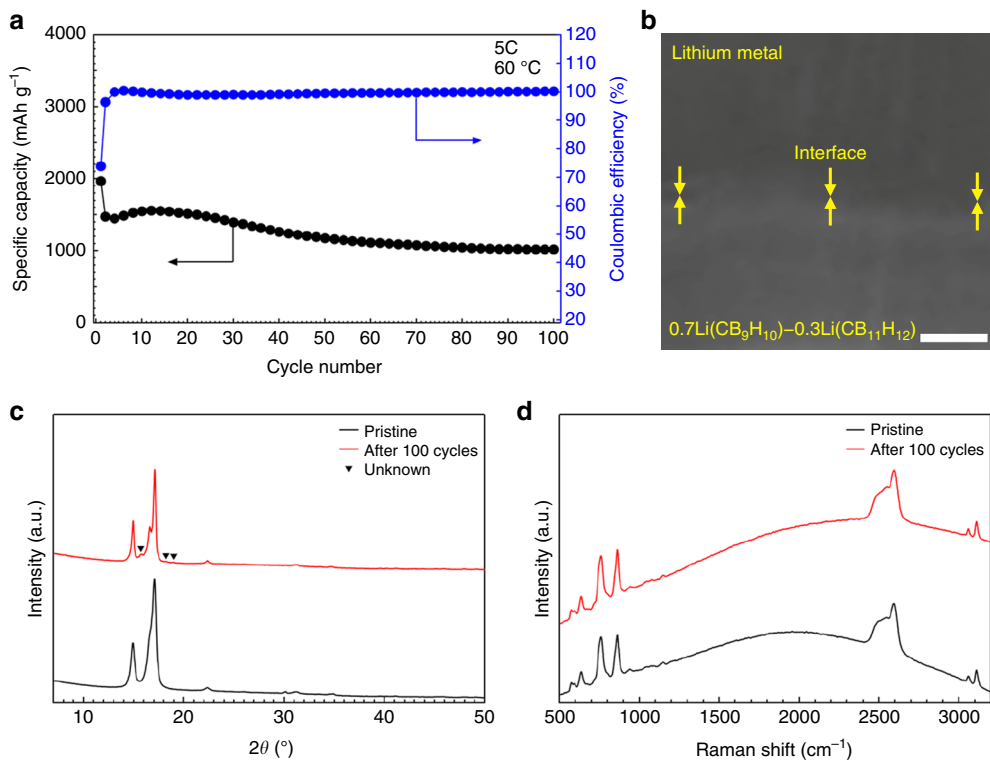


Fig. 6 Stability of 0.7Li(CB₉H₁₀)-0.3Li(CB₁₁H₁₂) during prolonged cycling. **a**, Cycling performance of discharge capacity and coulombic efficiency for a discharging rate of 5 C and a charging rate of 1 C at 60 °C. **b**, FE-SEM image of the 0.7Li(CB₉H₁₀)-0.3Li(CB₁₁H₁₂)/Li interface after 100 cycles. **c**, XRD patterns and **d**, Raman profiles of 0.7Li(CB₉H₁₀)-0.3Li(CB₁₁H₁₂) before and after 100 cycles. A small amount of an unknown phase was detected in the XRD pattern. Scale bar, 20 μm in **b**.

method over a temperature range of 25–110 °C K with applied frequencies of 4 Hz–1 MHz using a frequency response analyzer (3532-80, HIOKI). Lithium self-diffusion coefficients were estimated using the PFG stimulated-echo method of ⁷Li NMR with a Bruker Avance 400 NMR spectrometer equipped with a Bruker Diff60 probe operating at a resonance frequency of 155.6 MHz.

Stability evaluation. The electrochemical stability was evaluated by CV (1470E, Solartron Analytical) using a Mo/0.7Li(CB₉H₁₀)-0.3Li(CB₁₁H₁₂)/Li cell in a scan range of −0.1 to 5 V (vs. Li⁺/Li). The interfacial resistance between 0.7Li(CB₉H₁₀)-0.3Li(CB₁₁H₁₂) and lithium metal was examined with a frequency response analyzer (3532-80, Hioki) using a Li/0.7Li(CB₉H₁₀)-0.3Li(CB₁₁H₁₂)/Li cell. Lithium plating/stripping cycling was conducted with a Li/0.7Li(CB₉H₁₀)-0.3Li(CB₁₁H₁₂)/Li cell at a current density of 0.2 mA cm⁻² using a battery tester (580 Battery Test System, Scribner Associates). For the symmetric Li/0.7Li(CB₉H₁₀)-0.3Li(CB₁₁H₁₂)/Li cell, a 0.7Li(CB₉H₁₀)-0.3Li(CB₁₁H₁₂) pellet with a larger thickness (0.14 cm) than that (0.10 cm) used for the conductivity evaluation was prepared to avoid lithium–lithium shorting. Mo foil (Nilaco) and lithium foil (Honjo Metal) were used as electrodes of the Mo/0.7Li(CB₉H₁₀)-0.3Li(CB₁₁H₁₂)/Li and Li/0.7Li(CB₉H₁₀)-0.3Li(CB₁₁H₁₂)/Li cells. For cell fabrication, 50–70 mg of the 0.7Li(CB₉H₁₀)-0.3Li(CB₁₁H₁₂) powder was placed into a 10-mm-diameter Teflon guide and uniaxially pressed at 38.4 MPa. The electrodes were transferred onto the pressed sample still present in the Teflon guide and uniaxially pressed again at 153.6 MPa to prepare pellet-type cells. The cross-section of the 0.7Li(CB₉H₁₀)-0.3Li(CB₁₁H₁₂)/Li interface was observed using FE-SEM (S-3400N, Hitachi). To prevent lithium metal from sticking to the cell, Cu foil was inserted between the lithium metal and cell. The FE-SEM specimen for the cross-section observation was prepared using a dual-beam focused ion beam (FIB, FB2200, Hitachi).

Battery assembly and electrochemical test. All of the cell preparation processes were conducted under an Ar atmosphere inside a glove box. Discharge–charge experiments were performed with a S/0.7Li(CB₉H₁₀)-0.3Li(CB₁₁H₁₂)/Li cell. For cathode composite fabrication, an S–C composite was first prepared. Elemental S (Sigma-Aldrich), Ketjen black (KB, ECP600JD, Lion Corp.), and Maxsorb (MSC-30, Kansai Coke and Chemicals Co., Ltd) were weighted in a 50:25:25 (wt %) ratio and ball-milled at 400 rpm for 20 h under an Ar atmosphere²². The S–C composite and 0.7Li(CB₉H₁₀)-0.3Li(CB₁₁H₁₂) powders were then mixed at a 1:1 mass ratio using an agate mortar and pestle for 15 min and used as the cathode composite. For cell fabrication, 50–70 mg of the 0.7Li(CB₉H₁₀)-0.3Li(CB₁₁H₁₂) powder was placed into a 10-mm-diameter Teflon guide and uniaxially pressed

at 38.4 MPa. Subsequently, ~8 mg of the cathode composite powder and lithium foil anode were transferred onto opposite sides of the electrolyte still present in the Teflon guide and uniaxially pressed again at 153.6 MPa to prepare pellet-type cells. The cells were cycled in the voltage range of 1.0–2.5 V (vs. Li⁺/Li) using a battery tester (580 Battery Test System, Scribner Associates). The C-rate in this study is defined based on 1 C = 1672 mA g⁻¹. For the calculation of the gravimetric capacities and currents, only the mass of the S cathode material was taken into account. The specific energy density was calculated using

$$E = \frac{1}{m} \int_0^T i \times V dt \quad (1)$$

where *i* is the static current, *V* is the cell voltage, *T* is the discharging time required to reach the cutoff voltage, and *m* is the mass of the S cathode material.

Data availability

The data that support the findings of this study are available from the corresponding authors upon reasonable request.

Received: 12 September 2018 Accepted: 17 February 2019

Published online: 06 March 2019

References

- Kamaya, N. et al. A lithium superionic conductor. *Nat. Mater.* **10**, 682–686 (2011).
- Seino, Y. et al. A sulphide lithium super ion conductor is superior to liquid ion conductors for use in rechargeable batteries. *Energy Environ. Sci.* **7**, 627–631 (2014).
- Han, X. et al. Negating interfacial impedance in garnet-based solid-state Li metal batteries. *Nat. Mater.* **16**, 572–579 (2017).
- Kato, Y. et al. High-power all-solid-state batteries using sulfide superionic conductors. *Nat. Energy* **1**, 16030 (2016).
- Sun, Y. et al. Superionic conductors: $\text{Li}_{10+\delta}[\text{Sn}_y\text{Si}_{1-y}]_{1+\delta}\text{P}_{2-\delta}\text{S}_{12}$ with a $\text{Li}_{10}\text{GeP}_2\text{S}_{12}$ -type structure in the $\text{Li}_3\text{PS}_4\text{-Li}_4\text{SnS}_4\text{-Li}_4\text{Si}_4$ quasi-ternary system. *Chem. Mater.* **29**, 5858–5864 (2017).

6. Mizuno, F., Hayashi, A., Tadanaga, K. & Tatsumisago, M. New, highly ion-conductive crystals precipitated from Li₂S-P₂S₅ glasses. *Adv. Mater.* **17**, 918–921 (2005).
7. Deiseroth, H. J. et al. Li₄PS₅X: a class of crystalline Li-rich solids with an unusually high Li⁺ mobility. *Angew. Chem. Int. Ed.* **47**, 755–758 (2008).
8. Yu, C., Eijck, Lv, Ganapathy, S. & Wagemaker, M. Synthesis, structure and electrochemical performance of the argyrodite Li₄PS₅Cl solid electrolyte for Li-ion solid state batteries. *Electrochim. Acta* **215**, 93–99 (2016).
9. Inaguma, Y. et al. High ionic conductivity in lithium lanthanum titanate. *Solid State Commun.* **86**, 689–693 (1993).
10. Kim, S. et al. Low temperature synthesis and ionic conductivity of the epitaxial Li_{0.17}La_{0.61}TiO₃ film electrolyte. *Crystengcomm* **16**, 1044–1049 (2014).
11. Murugan, R., Thangadurai, V. & Weppner, W. Fast lithium ion conduction in garnet-type Li₇La₃Zr₂O₁₂. *Angew. Chem. Int. Ed.* **46**, 7778–7781 (2007).
12. Kim, S., Hirayama, M., Taminato, S. & Kanno, R. Epitaxial growth and lithium ion conductivity of lithium-oxide garnet for an all solid-state battery electrolyte. *Dalton Trans.* **42**, 13112–13117 (2013).
13. Mo, Y., Ong, S. P. & Ceder, G. First principles study of the Li₁₀GeP₂S₁₂ lithium super ionic conductor material. *Chem. Mater.* **24**, 15–17 (2012).
14. Cheng, L. et al. The origin of high electrolyte-electrode interfacial resistances in lithium cells containing garnet type solid electrolytes. *Phys. Chem. Chem. Phys.* **16**, 18294–18300 (2014).
15. Zhu, Y., He, X. & Mo, Y. Origin of outstanding stability in the lithium solid electrolyte materials: insights from thermodynamic analyses based on first-principles calculations. *ACS Appl. Mater. Interfaces* **7**, 23685–23693 (2015).
16. Oh, G. et al. Bulk-type all solid-state batteries with 5 V class LiNi_{0.5}Mn_{1.5}O₄ cathode and Li₁₀GeP₂S₁₂ solid electrolyte. *Chem. Mater.* **28**, 2634–2640 (2016).
17. Suzuki, K. et al. High cycle capability of all-solid-state lithium–sulfur batteries using composite electrodes by liquid-phase and mechanical mixing. *ACS Appl. Mater. Interfaces* **1**, 2373–2377 (2018).
18. Tao, Y. et al. Lithium superionic conducting oxysulfide solid electrolyte with excellent stability against lithium metal for all-solid-state cells. *J. Electrochem. Soc.* **163**, A96–A101 (2015).
19. Zhang, Z. et al. Interface re-engineering of Li₁₀GeP₂S₁₂ electrolyte and lithium anode for all-solid-state lithium batteries with ultralong cycle life. *ACS Appl. Mater. Interfaces* **10**, 2556–2565 (2018).
20. Unemoto, A. et al. Stable interface formation between TiS₂ and LiBH₄ in bulk-type all-solid-state lithium batteries. *Chem. Mater.* **27**, 5407–5416 (2015).
21. Mohtadi, R. & Orimo, S. The renaissance of hydrides as energy materials. *Nat. Rev. Mater.* **2**, 16091 (2017).
22. Unemoto, A. et al. Development of bulk-type all-solid-state lithium-sulfur battery using LiBH₄ electrolyte. *Appl. Phys. Lett.* **105**, 083901 (2014).
23. Kim, S. et al. Fast lithium-ion conduction in atom-deficient *closo*-type complex hydride solid electrolytes. *Chem. Mater.* **30**, 386–391 (2018).
24. Tang, W. S. et al. Liquid-like ionic conduction in solid lithium and sodium monocarba-*closoborates* near or at room temperature. *Adv. Energy Mater.* **6**, 1502237 (2016).
25. Sethio, D., Daku, L. M. L. & Hagemann, H. Computational study of the vibrational spectroscopy properties of boron-hydrogen compounds: Mg(B₃H₈)₂, CB₉H₁₀[−] and CB₁₁H₁₂[−]. *Int. J. Hydrg. Energy* **42**, 22496–22501 (2017).
26. Ikeshoji, T. et al. Diffuse and doubly split atom occupation in hexagonal LiBH₄. *Appl. Phys. Lett.* **95**, 221901 (2009).
27. Lu, Z. & Ciucci, F. Structural origin of the superionic Na conduction in Na₂B₁₀H₁₀ *closoborates* and enhanced conductivity by Na deficiency for high performance solid electrolytes. *J. Mater. Chem. A* **4**, 17740–17748 (2016).
28. Kweon, K. E. et al. Structural, chemical, and dynamical frustration: origins of superionic conductivity in *closoborate* solid electrolytes. *Chem. Mater.* **29**, 9142–9153 (2017).
29. Dimitrieva, M. et al. Carbon incorporation and anion dynamics as synergistic drivers for ultrafast diffusion in superionic LiCB₁₁H₁₂ and NaCB₁₁H₁₂. *Adv. Energy Mater.* **8**, 1703422 (2018).
30. Okazaki, H. Deviation from the Einstein relation in average crystals self-diffusion of Ag⁺ ions in α -Ag₂S and α -Ag₂Se. *J. Phys. Soc. Jpn.* **23**, 355–360 (1967).
31. Kuwata, N. et al. Lithium diffusion coefficient in amorphous lithium phosphate thin films measured by secondary ion mass spectroscopy with isotope exchange methods. *Solid State Ion.* **294**, 59–66 (2016).
32. He, X., Zhu, Y. & Mo, Y. Origin of fast ion diffusion in super-ionic conductors. *Nat. Commun.* **8**, 15893 (2017).
33. Song, J. Y., Wang, Y. Y. & Wan, C. C. Review of gel-type polymer electrolytes for lithium-ion batteries. *J. Power Sources* **77**, 183–197 (1999).
34. Tsai, C. et al. Li₇La₃Zr₂O₁₂ interface modification for Li dendrite prevention. *ACS Appl. Mater. Interfaces* **8**, 10617–10626 (2016).
35. Sharafi, A. et al. Characterizing the Li-Li₇La₃Zr₂O₁₂ interface stability and kinetics as a function of temperature and current density. *J. Power Sources* **302**, 135–139 (2016).
36. Liu, T. et al. Achieving high capacity in bulk-type solid-state lithium ion battery based on Li_{6.75}La₃Zr_{1.75}Ta_{0.25}O₁₂ electrolyte: interfacial resistance. *J. Power Sources* **324**, 349–357 (2016).
37. Buschmann, H. et al. Structure and dynamics of the fast lithium ion conductor “Li₇La₃Zr₂O₁₂”. *Phys. Chem. Chem. Phys.* **13**, 19378–19392 (2011).
38. Yao, X. et al. High-performance all-solid-state lithium-sulfur batteries enabled by amorphous sulfur-coated reduced graphene oxide cathodes. *Adv. Energy Mater.* **7**, 1602923 (2017).
39. He, L. Q. et al. Synthesis of a bimetallic dodecaborate LiNaB₁₂H₁₂ with outstanding superionic conductivity. *Chem. Mater.* **27**, 5483–5486 (2015).
40. Tang, W. S. et al. Stabilizing superionic-conducting structures via mixed-anion solid solutions of monocarba-*closoborates*. *ACS Energy Lett.* **1**, 659–664 (2016).
41. Matsuo, M., Nakamori, Y. & Orimo, S. Lithium superionic conduction in lithium borohydride accompanied by structural transition. *Appl. Phys. Lett.* **91**, 224103 (2007).
42. Maekawa, H. et al. Halide-stabilized LiBH₄, a room-temperature lithium fast-ion conductor. *J. Am. Chem. Soc.* **131**, 894–895 (2009).
43. Li, W. et al. Li⁺ ionic conductivities and diffusion mechanisms in Li-based imides and lithium amide. *Phys. Chem. Chem. Phys.* **14**, 1596–1606 (2012).
44. Oguchi, H. et al. Lithium-ion conduction in complex hydrides LiAlH₄ and Li₃AlH₆. *J. Appl. Phys.* **107**, 096104 (2010).
45. Matsuo, M. et al. Complex hydrides with (BH₄)[−] and (NH₂)[−] anions as new lithium fast-ion conductors. *J. Am. Chem. Soc.* **131**, 16389–16391 (2009).
46. Tang, W. S. et al. Unparalleled lithium and sodium superionic conduction in solid electrolytes with large monovalent cage-like anions. *Energy Environ. Sci.* **8**, 3637–3645 (2015).

Acknowledgements

This work was supported by JSPS KAKENHI (Grant-in-Aid for Research Activity Start-up, 17H06519 and Grants-in-Aid for Scientific Research on Innovative Areas “Hydrogenomics”, JP18H05513 and JP18H05518), the Collaborative Research Center on Energy Materials in IMR (E-IMR), and Advanced Target Project-4 of WPI-AIMR, Tohoku University. The authors would like to thank H. Ohmiya and N. Warifune for technical assistance (Tohoku University).

Author contributions

S.K. designed the research. S.K. carried out the syntheses, measurements, and data analyses. H.O. assisted in the electrochemical measurements. N.T. assisted in the Raman spectroscopy measurements. T.S. assisted in the phase analyses using XRD patterns. S.T. and T.O. participated in discussions of the results. D.A., N.K. and J.K. performed the NMR measurements. S.K. wrote the manuscript. S.K. and S.O. supervised the research. All authors discussed the results and commented on the manuscript.

Additional information

Supplementary Information accompanies this paper at <https://doi.org/10.1038/s41467-019-09061-9>.

Competing interests: The authors declare no competing interests.

Reprints and permission information is available online at <http://npg.nature.com/reprintsandpermissions/>

Journal peer review information: *Nature Communications* thanks the anonymous reviewers for their contribution to the peer review of this work. Peer reviewer reports are available.

Publisher's note: Springer Nature remains neutral with regard to jurisdictional claims in published maps and institutional affiliations.



Open Access This article is licensed under a Creative Commons Attribution 4.0 International License, which permits use, sharing, adaptation, distribution and reproduction in any medium or format, as long as you give appropriate credit to the original author(s) and the source, provide a link to the Creative Commons license, and indicate if changes were made. The images or other third party material in this article are included in the article's Creative Commons license, unless indicated otherwise in a credit line to the material. If material is not included in the article's Creative Commons license and your intended use is not permitted by statutory regulation or exceeds the permitted use, you will need to obtain permission directly from the copyright holder. To view a copy of this license, visit <http://creativecommons.org/licenses/by/4.0/>.